Kinetic simulations of the interruption of large-amplitude shear-Alfvén waves in a high-β plasma

J. Squire[*]

Theoretical Astrophysics, 350-17, California Institute of Technology, Pasadena, CA 91125, USA and
Walter Burke Institute for Theoretical Physics, Pasadena, CA 91125, USA

M. W. Kunz

Department of Astrophysical Sciences, Princeton University, 4 Ivy Lane, Princeton, New Jersey 08544, USA and
Princeton Plasma Physics Laboratory, PO Box 451, Princeton, NJ 08543, USA

E. Quataert

Astronomy Department and Theoretical Astrophysics Center, University of California, Berkeley, CA 94720, USA

A. A. Schekochihin

The Rudolf Peierls Centre for Theoretical Physics, University of Oxford, 1 Keble Road, Oxford, OX1 3NP, UK and
Merton College, Oxford OX1 4JD, UK

Using two-dimensional hybrid-kinetic simulations, we explore the nonlinear "interruption" of standing and traveling shear-Alfvén waves in collisionless plasmas. Interruption involves a self-generated pressure anisotropy removing the restoring force of a linearly polarized Alfvénic perturbation, and occurs for wave amplitudes $\delta B_\perp/B_0 \gtrsim \beta^{-1/2}$ (where β is the ratio of thermal to magnetic pressure). We use highly elongated domains to obtain maximal scale separation between the wave and the ion gyroscale. For standing waves above the amplitude limit, we find that the large-scale magnetic field of the wave decays rapidly. The dynamics are strongly affected by the excitation of oblique firehose modes, which transition into long-lived parallel fluctuations at the ion gyroscale and cause significant particle scattering. Traveling waves are damped more slowly, but are also influenced by small-scale parallel fluctuations created by the decay of firehose modes. Our results demonstrate that collisionless plasmas cannot support linearly polarized Alfvén waves above $\delta B_\perp/B_0 \sim \beta^{-1/2}$. They also provide a vivid illustration of two key aspects of low-collisionality plasma dynamics: (i) the importance of velocity-space instabilities in regulating plasma dynamics at high β, and (ii) how nonlinear collisionless processes can transfer mechanical energy directly from the largest scales into thermal energy and microscale fluctuations, without the need for a scale-by-scale turbulent cascade.

Introduction.—Shear-Alfvén (SA) fluctuations are fundamental to magnetized plasma dynamics [1–3]. They are routinely observed in both laboratory and space plasmas [4, 5], and are the basis for modern theories of magnetohydrodynamic (MHD) turbulence [6–9]. They are also uniquely robust among plasma waves: their large-scale linear dynamics are nearly unmodified across both kinetic and fluid plasma models [2].

The purpose of this Letter is to explore, using hybrid-kinetic simulations, a notable exception to this robustness. We focus on linearly polarized large-scale SA waves above the "interruption limit" [10, 11],

$$\frac{\delta B_\perp}{B_0} \gtrsim \beta^{-1/2}, \qquad (1)$$

in a collisionless plasma. Here $\beta \equiv 8\pi p_0/B^2$ is the ratio of thermal pressure (p_0) to magnetic pressure (with B the field strength), B_0 is a background magnetic field, and $\delta B_\perp$ is an Alfvénically polarized field perturbation. As explained below, SA perturbations above the limit (1) rapidly (in less than one Alfvén time) transfer their mechanical energy from the largest scales to plasma microscales and thermal energy, without the help of a turbulent cascade.

The interruption of SA perturbations occurs due to the self-generation of *pressure anisotropy*, $\Delta p \equiv p_\perp - p_\parallel$ (where $p_\perp$

and $p_\parallel$ are the thermal pressures in the directions perpendicular and parallel to $\boldsymbol{B}$). Because particles' magnetic moments, $\mu = mv_\perp^2/2B$, are approximately conserved, pressure anisotropy is created whenever B changes in a weakly collisional plasma. If $\beta > 1$, the anisotropic momentum stress $\nabla\cdot(\Delta p\boldsymbol{BB}/B^2)$ can be as important as, or even dominate over, the magnetic tension $\nabla\cdot(\boldsymbol{BB})/4\pi$. This suggests that collisionless dynamics can differ significantly from MHD predictions, even for large-scale perturbations satisfying $\lambda \gg \rho_i$, $\tau \gg \Omega_i^{-1}$ (where ρ_i and Ω_i are the ion gyroradius and gyrofrequency, respectively).

"Interruption" occurs when the changing B in a linearly polarized SA oscillation creates an anisotropy $\Delta p = -B^2/4\pi$, which exactly offsets the magnetic tension and triggers the firehose instability on ion gyroscales [12–15]. Even at small wave amplitudes (if $\beta^{-1/2} < \delta B_\perp/B_0 \ll 1$), interruption is a nonlinear effect. Here, we study this behavior using hybrid kinetics (kinetic ions, fluid electrons), in three velocity and two spatial dimensions (the latter required to capture the oblique firehose instability). We focus on parallel standing or traveling SA waves in the limit of large scale separations, $\lambda_{\mathrm{mfp}} > \lambda_A \gg \rho_i$ (where λ_{mfp} and λ_A are ion mean-free path and the SA wavelength, respectively), as relevant to the intra-cluster medium [16, 17], hot accretion flows [18], and the inertial range in the solar wind [5, 19, 20]. Although the oblique firehose instability threshold differs slightly from the parallel
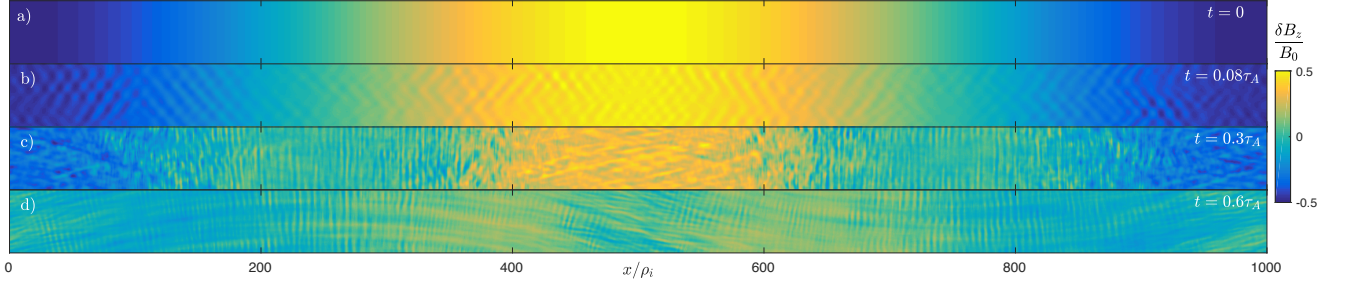
FIG. 1. Out-of-plane magnetic perturbation, $\delta B_z/B_0$, in a standing shear-Alfvén perturbation at $t = 0$, $t = 0.08\tau_A$, $t = 0.3\tau_A$, and $t = 0.6\tau_A$ ($\tau_A = 10^4\,\Omega_i^{-1}$ is the linear Alfvén period).

firehose threshold ($\Delta p = -B^2/4\pi$) [15, 21], in what follows, we organize our discussion around the latter because of its key importance for large-scale SA waves.

Hybrid-kinetic method.—By treating the electrons as an isothermal massless neutralizing fluid, the hybrid method removes electron kinetic scales, plasma oscillations, and light waves from the Vlasov-Maxwell equations, reducing simulation cost while retaining kinetic ion dynamics [22, 23]. The equations consist of (i) the collisionless Vlasov equation for the ion distribution function $f_i(\boldsymbol{x}, \boldsymbol{v}, t)$,

$$\frac{\partial f_i}{\partial t} + \boldsymbol{v} \cdot \frac{\partial f_i}{\partial \boldsymbol{x}} + \frac{q_i}{m_i}\left(\boldsymbol{E} + \frac{1}{c}\boldsymbol{v} \times \boldsymbol{B}\right) \cdot \frac{\partial f_i}{\partial \boldsymbol{v}} = 0; \qquad (2)$$

(ii) Faraday's law for the magnetic field,

$$\frac{\partial \boldsymbol{B}}{\partial t} = -c\nabla \times \boldsymbol{E}; \qquad (3)$$

and (iii), a generalized Ohm's law for the electric field,

$$\boldsymbol{E} + \frac{1}{c}\boldsymbol{u}_i \times \boldsymbol{B} = -\frac{T_e \nabla n_i}{en_i} + \frac{(\nabla \times \boldsymbol{B}) \times \boldsymbol{B}}{4\pi q_i n_i}. \qquad (4)$$

Here, q_i and m_i are the ion's charge and mass, $\boldsymbol{E}$ is the electric field, c is the speed of light, and T_e is the electron temperature. The ion density $n_i(\boldsymbol{x}) \equiv \int d\boldsymbol{v}\, f_i$ and bulk velocity $\boldsymbol{u}_i(\boldsymbol{x}) \equiv \int d\boldsymbol{v}\, \boldsymbol{v} f_i$ are calculated from f_i, thus closing the system.

We use the second-order-accurate particle-in-cell (PIC) code, *Pegasus* [24], to solve Eqs. (2)-(4). We employ the δf method [25], which evolves $\delta f = f - f_0$ rather than f itself, and take f_0 to be an isotropic Maxwellian. This reduces particle noise by $\sim (\delta f/f_0)^2$, making it optimal for simulation of high-β plasmas, where very small ($\ll 1/\beta$) deviations from a Maxwellian distribution must be accurately resolved.

Simulation set up.—We consider two specific initial conditions, which initially have variation only on large scales. These are (i) a parallel standing SA wave initiated by a magnetic perturbation, and (ii) a parallel traveling SA wave. We focus on the standing wave because of its relevance to situations where $\langle dB/dt \rangle \neq 0$, as would occur in Alfvénic turbulence (here $\langle \cdot \rangle$ represents a spatial average). Although also

important, we leave study of initial Alfvénic velocity perturbations to future work, due to the larger simulation domains required to capture the dynamics of the mirror instability [26, 27]. The initial ion distribution function is an isotropic Maxwellian with $T_e = T_i$ and we impose a background magnetic field $\boldsymbol{B} = B_0\hat{\boldsymbol{x}}$, with $\beta_i = 8\pi n_i T_i/B_0^2 = 100$. Each domain is of width $50\rho_i$ in the y direction and much longer (up to $L_x = 1000\rho_i$) in the x direction, to maximize scale separation between the SA wave and microscale dynamics. We use a spatial resolution of $\Delta x = 0.3125\rho_i$ and $N_{\mathrm{ppc}} = 4096$ particles per cell (ppc) for the two main simulations in this Letter. We initialize with a sinusoidal perturbation of wavelength $\lambda_A = L_x$ in the out-of-plane field, $\delta B_z = -\delta b\, B_0 \cos(2\pi x/\lambda_A)$, and, for the traveling wave, a corresponding velocity perturbation, $\delta u_z = \delta b\, v_A \cos(2\pi x/\lambda_A)$. In both cases, we take the wave amplitude $\delta b = 0.5$, which is well above the interruption limit $\delta b_{\max} \approx 2\beta^{-1/2}$ [10]. Within the MHD model, these initial conditions would create continuing sinusoidal SA oscillations of period $\tau_A = 2\pi/\omega_A = \sqrt{\beta_i}\lambda_A/\rho_i\Omega_i^{-1}$ (modified slightly by compressibility [11]).

Due to the wide range of time and space scales involved in this problem, careful numerical tests are crucial. In addition to previous *Pegasus* tests [24], we performed tests of the numerical parameters required to accurately propagate long-wavelength linear SA waves (with $\lambda_A/\rho_i = 50$ to 1000, $\delta b = 0.05$). These tests demonstrated that high ppc ($N_{\mathrm{ppc}} \propto \lambda_A/\rho_i$) is required for large wavelengths, due to the build up of PIC noise over long simulation times. For production runs, $N_{\mathrm{ppc}} = 4096$ was chosen based on these requirements. We also tested the convergence (with N_{ppc}) of nonlinear standing waves at $\lambda_A/\rho_i = 250$, and their dependence on λ_A/ρ_i over the range $\lambda_A/\rho_i = 125$ to 1000. We observed broadly similar dynamics over this range.

Shear-Alfvén standing wave.—Figure 1 shows the spatiotemporal evolution of δB_z for a standing SA wave with $\lambda_A/\rho_i = 1000$, $\omega_A/\Omega_i = 2\pi \times 10^{-4}$. The pictured snapshots are chosen to illustrate four distinct phases of nonlinear wave evolution. These are: (i) initial field decrease, which creates a negative anisotropy $\Delta p < -B^2/4\pi$, nullifying magnetic tension and triggering the firehose instability; (ii) eruption of oblique firehose modes [14, 15, 28] which push the wave back
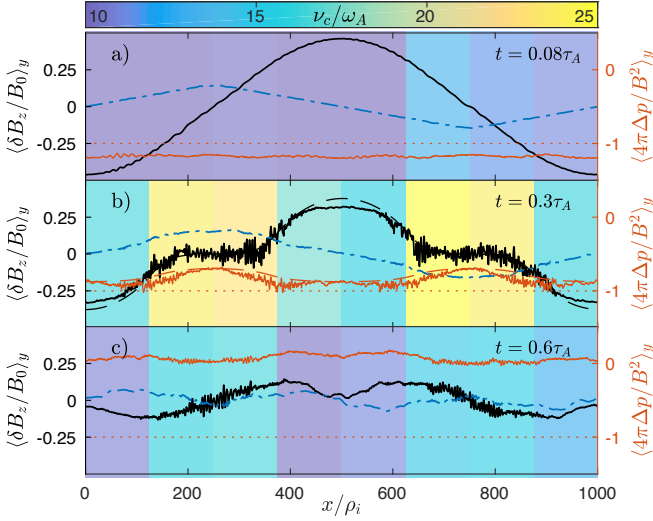
FIG. 2. Evolution of the standing wave from Fig. 1: we show the y-averaged $\delta B_z/B_0$ (black line, left axis), $\delta u_z/v_A$ (blue dot-dashed line, left axis), and firehose parameter $4\pi\Delta p/B^2$ (red, right axis; the dotted red line shows $\Delta p = -B^2/4\pi$), at the times illustrated in Figs. 1(b)–(d). The background color shows the effective collisionality ν_c/ω_A caused by particle scattering from microscale fluctuations, measured over the time intervals $t/\tau_A \in [0.07, 0.15]$ (a), $t/\tau_A \in [0.2, 0.4]$ (b), and $t/\tau_A \in [0.55, 0.65]$ (c). In (b), we also show (dashed lines) $\delta B_z/B_0$ and $4\pi\Delta p/B^2$ for a decaying SA standing wave in a Braginskii model at $\beta = 100$, $\nu_c/\omega_A \approx 10$ ($\delta u_z/v_A$ is omitted for clarity).

above $4\pi\Delta p/B^2 = -1$; (iii) decay of oblique firehose modes into $k_\perp = 0$, $k_\parallel\rho_i \sim 1$ Alfvénic fluctuations that strongly scatter particles and cause the large-scale δB_z to decay; and (iv), dissolution of the wave into SA waves below the limit (1), which oscillate freely without causing the plasma to reach the firehose limit. Of these stages, (iii) is notably different from the predictions of 1-D Landau-fluid (LF) models [10, 11].

Figure 2 shows 1-D (y-averaged) wave profiles. As magnetic tension causes δB_z (and thus B) to decrease, Δp decreases also, reaching $\Delta p = -B^2/4\pi$ at $t \approx 0.07\tau_A$. Due to heat fluxes smearing Δp along $\boldsymbol{B}$ [11], $\Delta p/B^2$ is nearly homogeneous in space [Fig. 2(a)], and oblique firehose modes erupt suddenly across the entire wave at once [Fig. 1(b)]. At this point the large-scale wave has no restoring force because magnetic tension is nullified by the anisotropic-pressure stress. However, with B now *increasing* due to the fast-growing firehose modes, Δp increases quickly above $\Delta p > -B^2/4\pi$ (by $t \approx 0.085\tau_A$), where it stays until the SA wave has decayed.

The subsequent evolution of the oblique firehose modes controls the large-scale SA wave dynamics. If these residual modes (now in the stable regime) scatter particles sufficiently fast, over sufficiently long times, δB_z can decay with $\Delta p \approx -B^2/4\pi$; if they do not (e.g., if they are resonantly damped [18, 26, 30]), δB_z cannot decrease further, as suggested by LF calculations [10]. The anisotropy dynamics, which controls the firehose modes' evolution, varies in space. Near the wave nodes, where $S = |\nabla\boldsymbol{u}| \approx 0$ and $\delta B_z \approx 0$,
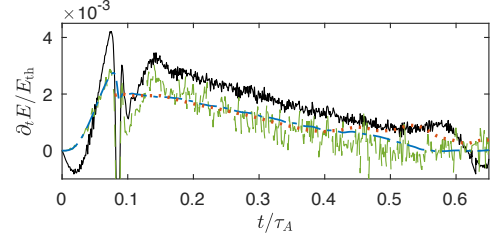

FIG. 3. Plasma heating due to the standing wave in Fig. 1. We compare the rate of change of thermal energy $\partial_t E_{\text{th}} = \int d\boldsymbol{x}\, n_i \sum_r \partial_t(\Pi_{rr}/n_i)/2$ (black line; Π_{rs} is the pressure tensor), with mechanical heating $-\int d\boldsymbol{x} \sum_{rs}\Pi_{rs}\nabla_r u_s$ (green dashed line), heating from the large-scale SA wave $\int d\boldsymbol{x}\,\Delta\bar{p}\,\hat{b}_x\hat{b}_z\partial_x\bar{u}_z$ (blue dot-dashed line; here $\bar{}$ denotes a filter that smooths fluctuations with $k\rho_i \gtrsim 0.25$), and the approximate viscous heating [29] from the SA wave after interruption $\nu_c^{-1}\int d\boldsymbol{x}\,\bar{p}_\parallel(\hat{b}_x\hat{b}_z\partial_x\bar{u}_z)^2$ (red dotted line; we use $\nu_c/\omega_A \approx 10$ as in Fig. 2). We normalize by E_{th} and use units of τ_A (note the small rates, due to the high β). The initial $\partial_t E_{\text{th}} < 0$ is due to the creation of $\boldsymbol{E}$ fluctuations (because of particle noise).

the anisotropy is not driven by a large-scale dB/dt and can freely decay [26, 31–33]. Near the wave antinodes, where $S \sim \beta^{-1/2}\omega_A \approx 6\times10^{-5}\Omega_i$ [11] and $\delta B_z \neq 0$, the anisotropy is continuously driven by the decreasing field [26, 28, 34–36].

Surprisingly, it is the small-scale modes at the SA wave nodes—the *least* firehose-unstable regions (with $4\pi\Delta p/B^2 \approx -0.7$)—that cause the strongest particle scattering. This is illustrated by the background color in Fig. 2, which shows the effective ion collisionality ν_c/ω_A as a function of space, measured by calculating the time it takes for μ to change by a factor of 1.2 for 2048 sample ions [37]. There is a clear change from weak homogenous scattering during the initial excitation of oblique firehose modes, to stronger scattering, localized around the SA wave nodes, at later times. The cause for this behavior is the decay of oblique firehose modes into $k_\parallel\rho_i \sim 1$, $k_\perp \sim 0$ Alfvénic modes, which can be seen clearly in Fig. 1(c). These parallel modes decay slowly (they are nonlinearly stabilized against cyclotron damping [38, 39]), as indicated by their presence after the large-scale SA wave has decayed and $\Delta p \sim 0$ [Fig. 1(d)]. Surprisingly, oblique firehose fluctuations at the wave antinodes contribute less to the scattering, even though they are continuously driven by a decreasing field. Scalings in [26] suggest that growing firehose modes in this shear flow would cause strong particle scattering after a secular growth phase of length $t \sim (\Omega_i\beta/S)^{1/2}\Omega_i^{-1} \approx 0.125\tau_A$; however, this does not occur here because the anisotropy driving, $d\Delta p/dt \sim -|S|p_0$, is balanced by scattering from the SA wave nodes.

The particle scattering governs the subsequent evolution of the large-scale SA wave. Because $\omega_A \ll \nu_c \ll \Omega_i$, the wave dynamics are no longer collisionless; they are instead in a regime that resembles the Braginskii collisional limit [40] and the SA wave behaves as discussed in [11], Sec. 4.1. We illustrate the qualitative similarity in Fig. 2(b), which also shows δB_z and $4\pi\Delta p/B^2$ for a wave governed
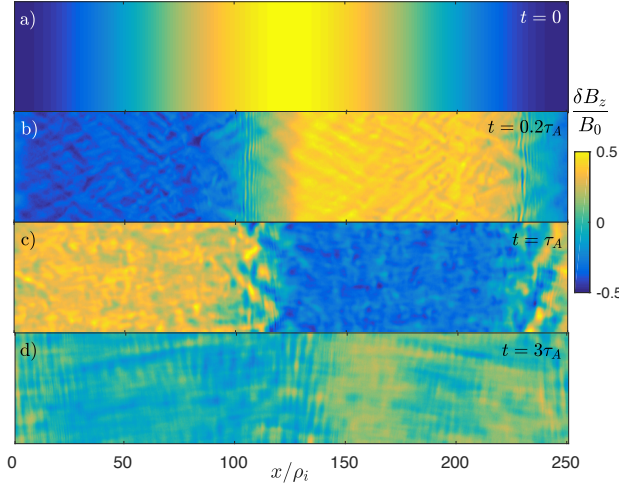
FIG. 4. Out-of-plane magnetic perturbation $\delta B_z/B_0$ for a SA traveling wave with $\lambda_A = 250\rho_i$ at a succession of times in its evolution. Note the significant decay of the wave by $t = 3\tau_A$.

FIG. 5. (a) Scattering rate ν_c/ω_A of the traveling wave in Fig. 4 as a function of x and t. The grey lines follow the wave fronts (this is close to where Δp is most negative). (b) Time evolution of $\langle 4\pi\Delta p/B^2 \rangle$. The shaded region indicates the range of $4\pi\Delta p/B^2$ seen across the wave profile, to illustrate when the wave can excite firehose modes. (c) Energy of the magnetic perturbation $E_{\delta B} = \int dx\, \delta B_z^2/8\pi$ (blue) and kinetic energy $E_{\delta u} = \int dx\, \rho\delta u_z^2/2$ (red), normalized by $E_0 = \int dx\, B_0^2/8\pi$. In panels (b) and (c), we also plot the results from an equivalent Landau-fluid simulation [11] (dashed lines), for comparison.

by the Braginskii model (including heat fluxes; see App. B of [11]). The "humped" shape of the SA wave occurs because the perturbation splits into regions where $4\pi\Delta p \approx -B^2$ and $d\delta B_z/dt < 0$ (around the antinodes), and regions where $4\pi\Delta p > -B^2$ and $\delta B_z = 0$ (these spread from the nodes). The wave decay rate is determined by ν_c [11], which is sufficiently large [$\nu_c/\omega_A \sim \beta(\delta B_\perp/B_0)^2$] that the wave decays within one Alfvén time. Note, however, that the dynamics are not identical to the Braginskii model: $\nu_c \neq 0$ only *after* the excitation of firehose modes. We note parenthetically that the wave decay generates a δB_y perturbation (see Fig. 1). Unfortunately, at this scale separation, it is unclear whether this effect is appreciably stronger than the δB_y generation that occurs in a linear SA wave due to gyroviscosity.

As the large-scale SA wave decays, it heats the plasma. This process does not involve a turbulent cascade, but rather a direct transfer of large-scale mechanical energy into thermal energy. This heating is essentially viscous dissipation of the wave, with particle scattering from microscale fluctuations controlling the effective viscosity and making the process irreversible. In Fig. 3, we compare the measured $\partial_t E_{\mathrm{th}}$ with heating due to the SA wave decay. Although the agreement is not perfect, due to spurious grid heating [41] (tests at $\lambda_A/\rho_i = 250$ show that this improves with ppc or reduced λ_A/ρ_i), the various stages of wave decay are evident; e.g., the sudden drop in $\partial_t E_{\mathrm{th}}$ as firehose fluctuations grow at $t/\tau_A \approx 0.08$, followed by heating as the large-scale $\delta B_\perp$ decays. Fig. 3 also shows that the overall energetics are well captured by considering only the large-scale dynamics, or by using the same effective collisionality as in Fig. 2(b). This supports closure models that approximate the effects of microinstabilities on large-scale dynamics without having to resolve the microscales.

Shear-Alfvén traveling wave.—Figures 4 and 5 illustrate the spatiotemporal evolution of the nonlinear SA traveling wave
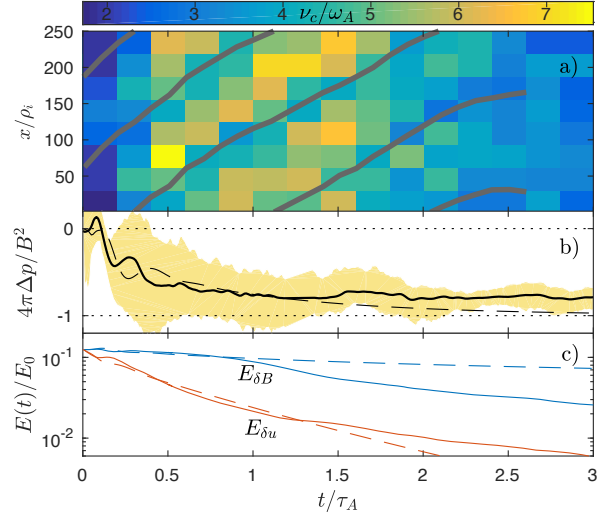
with $\lambda_A = 250\rho_i$. The initial dynamics differ from SA standing waves because $\langle dB/dt \rangle = 0$ for an unperturbed traveling wave, implying that global (spatially constant) pressure anisotropy is created only as the wave decays [10]. The evolution broadly follows the expectations of [10, 11], proceeding in 4 stages: (i) the spatially dependent dB/dt creates an anisotropy $\Delta p(x) \sim \beta^{1/2}\delta B_z^2 \sin(2k_\parallel x)$; (ii) this Δp damps the wave at a rate $\sim \int dx\, \Delta p\, d\ln B/dt$ [11, 42, 43] causing $\langle B \rangle$ to decrease and creating a global anisotropy $\langle \Delta p \rangle < 0$; (iii) the wave consequently slows down, with $\delta u_\perp$ decaying faster than $\delta B_\perp$; and (iv) the wave excites oblique firehose modes, which evolve and scatter particles in a similar manner to the standing wave, causing the large-scale SA wave to decay.

These stages can be seen clearly in Figs. 4 and 5. In particular, note the global $\langle \Delta p \rangle < 0$ that quickly develops [Fig. 5(b)] and the faster decay of kinetic compared to magnetic energy at early times [Fig. 5(c)]. After the initial drop in Δp, by $t/\tau_A \approx 0.3$, the wave starts exciting oblique firehose modes. In contrast to the standing wave, this occurs only in localized regions around the wavefronts (i.e., near where $\delta B_z = 0$), because $|dB/dt|$ (and thus $|\Delta p|$) is largest in these regions [see, e.g., Fig. 4(c) at $x/\rho_i \approx 110$ and the shading in Fig. 5(b)]. Following this excitation of firehose modes, Fig. 5(a) shows that the particle scattering is strongest behind the wavefronts. We interpret this as being due to the transition of oblique firehose modes into long-lived $k_\parallel\rho_i \sim 1$ Alfvénic modes, as occurred for the standing wave [these are clearly visible in Fig. 4(d)].

The scattering rate ν_c/ω_A is significantly lower than for the standing wave, which is likely because the firehose modes are excited only briefly in isolated regions of space, and the traveling wave's δB_z decays correspondingly more slowly. At earlier times, the large-scale SA wave evolution matches well the predictions from a 1-D LF model at $\beta_i = 100$ [11] (dashed lines in Fig. 5). At later times, particle scattering allows the large-scale $\delta B_\perp$ to decay (maintaining $\langle \Delta p \rangle < 0$ requires $\langle dB/dt \rangle < 0$ if $\nu_c \neq 0$), and the wave's final stages are similar to the standing wave.

Discussion.—We have presented hybrid-kinetic simulations of large-amplitude SA waves in a collisionless plasma. These simulations verify, using a realistic model with kinetic ion dynamics, the result of [10]: linearly polarized shear-Alfvénic perturbations do not exist in their linear wave form above the amplitude limit $\delta B_\perp/B_0 \sim \beta^{-1/2}$. Our results also demonstrate the exceptional influence of microinstabilities on the dynamics of high-β collisionless plasmas even on large scales $\lambda_A \gg \rho_i$, viz., the SA wave dynamics depend strongly on how oblique firehose modes evolve as the plasma becomes stable ($\Delta p \gtrsim -B^2/4\pi$). In particular, we find that firehose fluctuations become parallel ($k_\perp = 0$) and move to smaller scales ($k_\parallel \rho_i \sim 1$), surviving throughout the large-scale $\delta B_\perp$ decay and scattering particles at a high rate. This causes SA standing-wave dynamics in a collisionless plasma to resemble those in a collisional (Braginskii) one [11]. For traveling waves, the initial evolution of the wave is effectively collisionless and matches analytic predictions [11]; however, once the wave builds up a global negative anisotropy, it also excites oblique firehose modes and the final stages of wave decay resemble the standing wave. For both standing and traveling waves, the simulations provide an interesting example of direct transfer of energy from the largest scales to thermal energy and microscale fluctuations, without a turbulent cascade.

Our simulations cannot fully address what occurs at yet higher λ_A/ρ_i. This will depend on how oblique firehose modes decay into parallel Alfvénic modes and scatter particles, physics that is currently poorly understood. That said, it is clear that SA wave interruption provides a robust mechanism for dissipating energy directly from large-scale perturbations into heat and microinstabilities. This strong deviation from the predictions of MHD models could significantly impact the turbulent dynamics of high-β weakly collisional plasmas [29]—a physical regime that is expected to be prevalent across a wide variety of astrophysical environments [5, 16–18]. Our results suggest that numerical modeling of these weakly collisional environments would be better off strongly damping large-amplitude SA waves, rather than letting them freely propagate. One concrete way to achieve this aim might be a LF model with pressure-anisotropy limiters [44] that enhance the collisionality to a rate that is determined by the large-scale Alfvén frequency. More work on developing and validating subgrid models of this kind is underway.

* jsquire@caltech.edu
[1] H. Alfvén, Nature **150**, 405 (1942).
[2] N. F. Cramer, *The Physics of Alfvén Waves* (John Wiley & Sons, 2011).
[3] G. I. Ogilvie, J. Plasma Phys. **82**, 205820301 (2016).
[4] W. Gekelman, S. Vincena, B. V. Compernolle, G. J. Morales, J. E. Maggs, P. Pribyl, and T. A. Carter, Physics of Plasmas **18**, 055501 (2011).
[5] R. Bruno and V. Carbone, Living Rev. Solar Phys. **10** (2013).
[6] P. Goldreich and S. Sridhar, Astrophys. J. **438**, 763 (1995).
[7] S. Boldyrev, Phys. Rev. Lett. **96**, 11502 (2006).
[8] A. A. Schekochihin, S. C. Cowley, W. Dorland, G. W. Hammett, G. G. Howes, E. Quataert, and T. Tatsuno, Astrophys. J. Supp. **182**, 310 (2009).
[9] A. Mallet and A. A. Schekochihin, Mon. Not. R. Astron. Soc. **466**, 3918 (2017).
[10] J. Squire, E. Quataert, and A. A. Schekochihin, Astrophys. J. Lett. **830**, L25 (2016).
[11] J. Squire, A. Schekochihin, and E. Quataert, (2017), arXiv:1701.03175 [physics.plasm-ph].
[12] R. C. Davidson and H. J. Völk, Phys. Fluids **11**, 2259 (1968).
[13] M. N. Rosenbluth, Los Alamos Sci. Lab. Rep. **LA-2030** (1956).
[14] P. H. Yoon, C. S. Wu, and A. S. de Assis, Phys. Fluids B **5**, 1971 (1993).
[15] P. Hellinger and H. Matsumoto, J. Geophys. Res **105**, 10519 (2000).
[16] M. S. Rosin, A. A. Schekochihin, F. Rincon, and S. C. Cowley, Mon. Not. R. Astron. Soc. **413**, 7 (2011).
[17] I. Zhuravleva, E. Churazov, A. A. Schekochihin, S. W. Allen, P. Arevalo, A. C. Fabian, W. R. Forman, J. S. Sanders, A. Simionescu, R. Sunyaev, A. Vikhlinin, and N. Werner, Nature **515**, 85 (2014).
[18] E. Quataert, Astrophys. J. **500**, 978 (1998).
[19] S. D. Bale, J. C. Kasper, G. G. Howes, E. Quataert, C. Salem, and D. Sundkvist, Phys. Rev. Lett. **103**, 211101 (2009).
[20] C. H. K. Chen, J. Plasma Phys. **82**, 535820602 (2016).
[21] K. G. Klein and G. G. Howes, Phys. Plasmas **22**, 032903 (2015).
[22] J. A. Byers, B. I. Cohen, W. C. Condit, and J. D. Hanson, J. Chem. Phys. **27**, 363 (1978).
[23] D. W. Hewett and C. W. Nielson, J. Chem. Phys. **29**, 219 (1978).
[24] M. W. Kunz, J. M. Stone, and X.-N. Bai, J. Comp. Phys. **259**, 154 (2014).
[25] Y. Chen and S. Parker, J. Comp. Phys. **189**, 463 (2003).
[26] S. Melville, A. A. Schekochihin, and M. W. Kunz, Mon. Not. R. Astron. Soc. **459**, 2701 (2016).
[27] F. Rincon, A. A. Schekochihin, and S. C. Cowley, Mon. Not. R. Astron. Soc. **447**, L45 (2015).

[28] M. W. Kunz, A. A. Schekochihin, and J. M. Stone, Phys. Rev. Lett. **112**, 205003 (2014).

[29] M. W. Kunz, A. A. Schekochihin, S. C. Cowley, J. J. Binney, and J. S. Sanders, Mon. Not. R. Astron. Soc. **410**, 2446 (2010).

[30] E. A. Foote and R. M. Kulsrud, Astrophys. J. **233**, 302 (1979).

[31] K. B. Quest and V. D. Shapiro, J. Geophys. Res **101**, 24457 (1996).

[32] A. A. Schekochihin, S. C. Cowley, R. M. Kulsrud, M. S. Rosin, and T. Heinemann, Phys. Rev. Lett. **100**, 081301 (2008).

[33] J. Seough, P. H. Yoon, and J. Hwang, Phys. Plasmas **22**, 012303 (2015).

[34] L. Matteini, S. Landi, P. Hellinger, and M. Velli, J. Geophys. Res.: Space Phys. **111**, A10101 (2006).

[35] P. Hellinger and P. M. Trávníček, J. Geophys. Res **113**, A10109 (2008).

[36] M. A. Riquelme, E. Quataert, and D. Verscharen, Astrophys. J. **824**, 123 (2016).

[37] We then rescale ν_c so that ν_c^{-1} measures factor-e changes in μ.

[38] S. P. Gary and S. Saito, J. Geophys. Res **108**, 373 (2003).

[39] S. P. Gary, J. Geophys. Res **109**, 1483 (2004).

[40] S. I. Braginskii, Rev. Plasma Phys. **1**, 205 (1965).

[41] C. K. Birdsall and A. B. Langdon, *Plasma Physics via Computer Simulation* (Adam Hilger, Bristol, England, 1991).

[42] M. A. Lee and H. J. Völk, Astrophys. Space. Sci. **24**, 31 (1973).

[43] R. M. Kulsrud, in *Astronomical Papers Dedicated to Bengt Stromgren*, edited by A. Reiz and T. Andersen (1978) pp. 317–326.

[44] P. Sharma, G. W. Hammett, E. Quataert, and J. M. Stone, Astrophys. J. Lett. **637**, 952 (2006).